Chemical Science

Accepted Manuscript

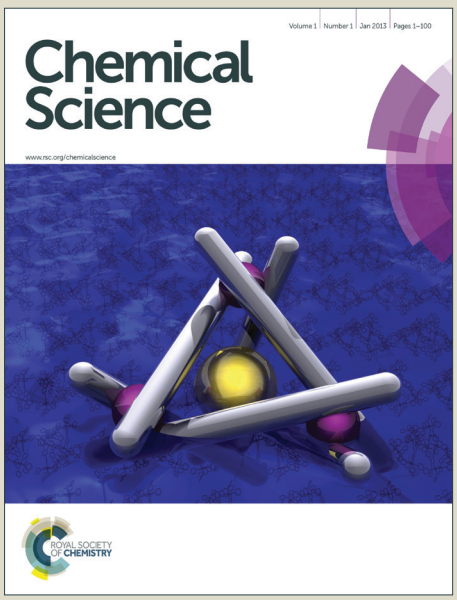

ROYAL SOCIETY OF CHEMISTRY

www.rsc.org/chemicalscience

Journal Name

RSCPublishing

ARTICLE

Wavelength Dependent Efficient Photoreduction of Redox Mediators Using Type II ZnSe/CdS Nanorod Heterostructures

Haiming Zhu, Zheyuan Chen, Kaifeng Wu and Tianquan Lian*

Cite this: DOI: 10.1039/x0xx00000x

Received ooth January 2012,
Accepted ooth January 2012

DOI: 10.1039/x0xx00000x

www.rsc.org/

One-dimensional quantum confined nanorod heterostructures (such as CdSe/CdS and ZnSe/CdS dot-in-rod) have been intensively investigated as light harvesting and charge separation materials for solar energy conversation because of the possibilities of rational incorporation of catalysts and achieving long distance charge separation though the selection of component materials with desired band alignment and dimension (diameter and length). To establish design principle for these materials, we have examined the redox mediator (methyl viologen, MV^{2+}) photoreduction process using ZnSe/CdS type II dot-in-rod nanorods. We show that the steady state MV^{2+} photoreduction quantum yields, in the presence of mercaptopropionic acid as electron donor, were 34% at 550 nm and 90% at 415 nm, respectively. Using transient absorption spectroscopy and time-resolved fluorescence decay, we followed the rates of electron and hole localization within the rod, interfacial transfer to acceptors, and charge recombination processes. It was shown that 550 nm excitation generated excitons in the charge transfer state with holes in the ZnSe seed and electrons at the CdS bulb region surrounding the seed. Electron transfer to MV^{2+} formed charge separated state with relatively small electron-hole spatial separation, leading to larger charge recombination loss and smaller steady-state quantum yield of MV^{2+} photoreduction. The excitons generated in the CdS rod region by 415 nm excitation underwent three charge separation pathways. The majority pathway led to long-distance charge separation with the electrons in the reduced MV^{2+} adsorbed on the rod and holes localized in the ZnSe seed, which suppressed recombination and resulted in the observed higher steady state quantum yield. We discuss possible approaches to control the branching ratios of different exciton localization/dissociation pathways and to improve the quantum efficiency of photoreduction.

Introduction

The advancement of solar-to-fuel conversion technologies requires not only efficient catalysts but also novel materials and approaches for light harvesting and charge separation. In recent years, quantum confined semiconductor nanocrystals have received intense interests as light harvesting and charge separation components in photocatalytic systems because of their tunable chemical, optical and electronic properties.[1] Compared with conventional single composition quantum dots (QDs), semiconductor nanoheterostructures, which combines two or more materials in one nanoscale system, provide additional opportunities for controlling their functionalities.[1a, 1c, 2] The electron and hole distributions and dynamics in heterostructures, which dictate their charge separation and photocatalytic properties, can be controlled by the conduction and valence band offsets of constituent materials as well as their geometries and dimensions. Among many reported morphologies, anisotropic one-dimensional nanorod (NR) heterostructures, e.g. ZnSe/CdS, CdSe/CdS dot-in-rods (DIRs), are particularly intriguing because of their potentials for long-distance charge separation and efficient photocatalysis.[1b, 1i, 3] For example, in a recent study, we reported a near unity quantum yield (QY) for redox mediator ($MV^{2+}/MV^{+\bullet}$) generation and efficient H_2 evolution with CdSe/CdS nanorods at 455 nm excitation, significantly higher than other nanostructures including CdSe/CdS core/shell QDs, CdSe quantum dots and CdS nanorods.[1b]

Due to the band offset between ZnSe and CdS, it is expected that in type II ZnSe/CdS dot-in-rod NRs, the lowest energy valence band (VB) hole is localized in the ZnSe seed and the lowest energy conduction band (CB) electron is located in the CdS rod.[4] Such spatial separation of CB electrons and VB holes, a key attribute of these type II and related quasi-type II CdSe/CdS NRs, is thought to lengthen the lifetime of charge separation.[1b, 1i, 3a, 3b, 3d, 5] However, recent experimental and

theoretical studies of CdSe/CdS quasi-type II NRs suggest that the electron wavefunction is largely localized near the hole (confined in the seed) due to strong e-h Coulomb interaction in these 1D structures.[4a, 6] Furthermore, the strong 1D exciton binding energy and presence of surface hole traps in CdS leads to multiple spatially separated long-lived exciton species in CdSe/CdS nanorods and the branching ratio among these species depends on the excitation wavelength.[6d, 6e] It is anticipated that such complex carrier distribution and excitation wavelength dependent exciton dynamics is likely a common feature of many dot-in-rod nanorods such as CdSe/CdS and ZnSe/CdS. Therefore, it is important to investigate its effect on the charge separation properties and photocatalytic performance of these nanorods.[1b, 1i, 3]

Herein, we investigated the excitation wavelength dependent performance and mechanism of MV^{2+} photo-reduction using type II ZnSe/CdS nanorods. This reaction was chosen because $MV^{2+}/MV^{+\bullet}$ is a well known redox couple (−0.45 vs NHE in aqueous solution) that can be further coupled with H_2 evolution[1b, 7] or CO_2 reduction[8] catalysts for direct solar-to-fuel conversion. ZnSe/CdS, with a clear type II band offsets between ZnSe and CdS, are chosen as a model for type II dot-in-rod NRs, offering an interesting comparison with the more extensively studied quasi-type II CdSe/CdS nanorods.[4] We report for the first time that under steady state illumination conditions and in the presence of electron donor (mercaptopropionic acid, 0.814 vs NHE[1e]), ZnSe/CdS nanorod showed dramatic wavelength dependent MV^{2+} photoreduction QY (~ 90% at 415nm and ~ 34% at 550 nm). Using transient absorption (TA) spectroscopy and time-resolved photoluminescence (PL) decay, we measured the rate of elementary steps, including exciton localization and trapping, interfacial electron and hole transfers, as well as the competing recombination processes, involved in the overall photoreduction process. We discuss how charge transfer pathways and their rates are influenced by the excitation wavelength dependent spatial distributions of electrons and holes and how they affect the observed steady state MV^{2+} photoreduction QYs.

Results and Discussion

Static Absorption and Emission Spectra ZnSe/CdS dot-in-rod NRs were synthesized by a seeded-growth approach starting with a ZnSe seed of ~ 2.9 nm in diameter (see Supporting Information S1).[4b, 9] Figure 1a shows a representative transmission electron microscopy (TEM) image of ZnSe/CdS NRs used in this study. According to the TEM image, the ZnSe/CdS NRs had an average length of 20.3 ± 2.5 nm and non-uniform diameters along the rod: a thinner rod (diameter ~ 3.7 nm) with a significantly thicker part ("bulb") near one end (diameter ~5.8 nm). This bulb feature has been observed in many seeded-grown ZnSe/CdS[4b, 4c] and CdSe/CdS nanorods,[6d, 10] and has been attributed to the growth of CdS shell surrounding the ZnSe or CdSe seed during the growth of the CdS rod.[4a, 4b, 10]

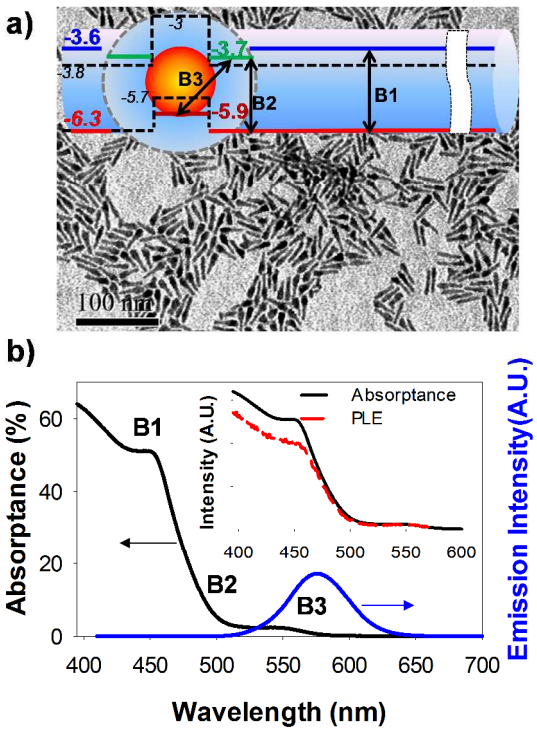

Figure 1. a) TEM image of ZnSe/CdS nanorods with an average length of 20.3 ± 2.5 nm. Inset: Schematic energy level diagram and key transitions in ZnSe/CdS NRs. b) UV-vis absorption (black solid line) and emission (blue solid line) spectra of ZnSe/CdS NRs in toluene solution. The y-axis is in the unit of (left) absorptance (the ratio of absorbed to incident light) for the absorption spectrum and (right) intensity for the emission spectrum. Inset: comparison of absorptance spectrum (black line) and photoluminescence excitation (PLE) spectrum (red dashed line). These spectra have been scaled to the same intensity at 550 nm.

The static UV-Vis absorption (in the unit of absorptance – the ratio of absorbed to incident photons) and emission spectra of ZnSe/CdS nanorod dispersed in toluene are displayed in Figure 1b. The ZnSe/CdS nanorod shows a lowest energy exciton absorption peak at 550 nm with emission centered at 575 nm. The amplitude of the Stokes shift (~60 meV) is similar to reported values of other ZnSe/CdS nanorods,[4b] although the origin of the shift remains unclear. This exciton band is well below the bandgap of either ZnSe or CdS and can be assigned to the lowest energy charge transfer (CT) transition from the lowest energy hole level ($1S_h$) in the ZnSe seed to lowest energy electron level in the CdS in this type II nanoheterostructure.[4d, 11] Here, we have assumed, for convenience, that the confinement potentials for electrons and holes in ZnSe seed and CdS bulb region still have spherical symmetry and the lowest energy electron and hole levels can be labelled as $1S_e$, and $1S_h$, respectively. It will be shown below that the electron level involved in the lowest energy CT band, depicted as B3 in Figure 1a inset, is the $1S_e$ level in the surrounding CdS bulb. The absorption spectrum also shows a clear exciton peak at ~ 457 nm, which can be attributed to quantum confined 1Σ excitonic transition in the CdS rod (B1 in

Figure 1a inset).[6d, 12] In addition to these two pronounced excitonic transitions, there is also an absorption feature at ~ 480 nm, which can be clearly observed from the transient absorption spectra (see below). This transition has a lower energy (shifted by ~130 meV) than the 1Σ peak in CdS rod region and can be assigned to the lowest energy transition in the CdS shell within the bulb region (B2 in Figure 1a inset). A similar bulb feature is observed in CdSe/CdS dot-in-rod NRs.[6d, 10] This indicates a smaller confinement energy in the bulb region, compared to the CdS rod, which is likely caused by its larger size and a much smaller confinement potential at the ZnSe/CdS interface (~0.7 V) than the CdS/solvent interface (~3.7 V). Its strength is small in the static absorption spectrum because of its relatively small volume compared to the CdS rod. From the TA spectra measured with direct excitation of the B3 transition at 555 nm (see below), the B2 bleach feature shows the same instantaneous formation and long-lived decay kinetics as the B3 bleach, indicating that these two transitions share the same electron level, i.e. the $1S_e$ level in the CdS shell in bulb region. From the B1 and B2 transition energy difference and electron/hole effective masses in CdS bulk material, we estimate that the lowest energy electron level in CdS rod is ~ 100 meV higher than that in the CdS bulb. Therefore, instead of extending throughout the whole rod, the lowest energy conduction band electron level for the ZnSe/CdS nanorod localizes in the CdS bulb region surrounding the ZnSe seed. Based on conduction/valence band edges of bulk ZnSe and CdS materials[1a] (black dashed lines in Figure 1a inset) and the energies of B1, B2 and B3 transitions, the lowest energy electron and hole levels throughout the nanorod can be deduced, which are shown in Figure 1a. We have neglected the electron-hole Columbic binding energy in this estimate.

The photoluminescence excitation (PLE) spectrum (detected at the emission maximum at 575 nm) of ZnSe/CdS nanorods is also shown and compared with the absorptance spectrum in Figure 1b inset. NR absorption at wavelength shorter than B2 is dominated by CdS rod because of its much larger volume and dielectric confinement effect.[13] If all excitons generated in the CdS rod can relax to form the B3 exciton, the ratio of PLE and absorptance should be unity throughout the absorption/PLE spectrum. The ratio of absorptance to PLE reflects the exciton localization efficiency from the state of excitation to the lowest energy B3 exciton state (the emissive state).[4b, 6d, 9a] As seen from Figure 1b, the normalized PLE intensity is about 17% smaller than the absorptance in CdS rod absorption region, indicating that only 83% of excitons created in the CdS nanorod region relaxes to the B3 exciton state in the seed. The remaining 17% are trapped at the CdS rod surface.[6d, 6e] Although this can also be caused by the presence of CdS nanorods without seed in the sample solution,[4b] its contribution is negligible according to the findings of the transient absorption studies to be discussed below.

Carrier Localization Dynamics in ZnSe/CdS Nanorod

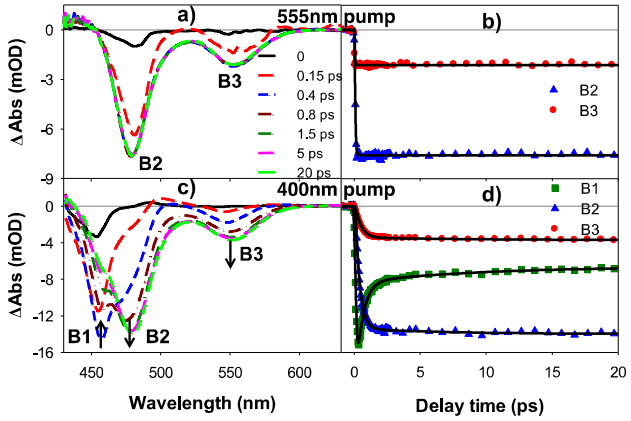

Figure 2. TA spectra and kinetics of ZnSe/CdS NRs in toluene at early delay time (0 - 20 ps) after 550 nm (upper panel) and 440 nm (lower panel) excitations. TA spectra at indicated delay times (a, c) and formation and decay kinetics of bleaches at B1 (green squares), B2 (blue triangles), and B3 (red circles) transitions (b, d). The black solid lines are fits according to a model described in the supporting information S2.

To support the above assignment and gain more insights into carrier distribution and relaxation dynamics, we performed femtosecond TA measurements on ZnSe/CdS nanorods. Excitation wavelength dependent TA studies have been proven to be an effective way to reveal the electronic structures and carrier dynamics in semiconductor nanoheterostructures.[5c, 6d, 14] The TA spectra and kinetics of ZnSe/CdS NRs at early delay times (0-20 ps) after 555 nm and 400 nm excitations are displayed in Figure 2 upper (a, b) and lower panel (c, d), respectively. To ensure that the TA kinetics can be compared with steady state photoreduction results, all TA measurements were carried out under single exciton conditions. Under such or lower excitation fluence, the contribution of multiple exciton state is negligible, and the exciton dynamics is not dependent on the fluence. The former is evident in Figure 2, which shows a lack of bi-exciton decay features on the 10 - 100 ps time scale.[14] TA signals of semiconductor nanocrystals contain two contributions: the state filling induced bleach of exciton bands (main component) and carrier induced Stark effect signals (minor component) that are derivatives of exciton features.[15] Similar to CdX (X=S, Se, Te) nanocrystals, the state filling induced TA signal in ZnSe/CdS nanorod is dominated by conduction band electrons with negligible hole contributions because of much denser hole states and valence band fine structures.[15] This assignment will be further validated by electron transfer study described below. Under 555 nm excitation, which is in resonance with lowest energy CT exciton transition (B3) in the bulb region, both B3 and B2 bleach features form instantaneously within the instrument response limit and decay in the same way in nanosecond timescale (not shown), confirming that these transitions share the same lowest energy electron level ($1S_e$) in the conduction band. The occupation of electrons in the $1S_e$ level doesn't lead to B1 bleach, indicating that its wavefunction is localized in bulb region without extending into the CdS rod.[4a]

Under 400 nm excitation, which generates excitons in the CdS rod domain, B1 bleach forms quickly (~ 50 fs formation time, see below) and then decays in the next few ps. Its decay leads to the growth of B2 and B3 bleach, indicating electron transport and localization from the lowest energy $1\sigma_e$ level in the CdS rod to the 1Se level in CdS bulb region. This electron localization process is clearly shown by the kinetics in Figure 2d. These kinetics can be well fitted by a multiexponential model described in S2 and the fitting parameters are listed in Table S1. According to the fit, both B2 and B3 bleaches show a biphasic rise with a ~ 91% fast component (417±42 fs for B2 and 487±61 fs for B3) and a ~ 9 % slower component (9.02±1.25 ps for B2 and 9.70±0.82 ps for B3), and a much slower decay on the nanosecond time scale (Figure S1). It should be noted that the spectral overlap contribution of B2 band at B1 bleach position has been accounted for in the fit since the line-shape of B2 bleach has been independently obtained in the TA spectra measured at 555 nm excitation (in which only the B2 bleach is present). The formation time of the B1 bleach, 53 (±11) fs, is assigned to the electron relaxation process from the initially excited 1π to 1σ level in the CdS NR.[6d, 12] The B1 bleach recovery contains two components: a fast and slow (>> 1ns) recovery components with 81(±4)% and 19(±4)% of the total amplitudes, respectively. The fast B1 bleach decay component can be well described by a bi-exponential decay process (0.498±0.057 ps, 89(±3)%; 9.09±1.02 ps, 11(±3)%) that agree well with the growth and B2, B3, indicating that ~ 81% of the initially created electrons in CdS rod decay to the bulb region. The ~ 19% slow component can be attributed to exciton that is localized to the CdS rod. This rod-to-bulb electron localization efficiency is consistent with the 83% rod exciton localization efficiency determined from the PLE measurement shown in Figure 1b. Similar competition of band alignment driven exciton localization and hole trapping induced exciton trapping has been reported in CdSe/CdS nanorods and tetrapods,[6d, 6e, 16 16-17] and has been attributed to local energetic heterogeneities and strong e-h interaction arose from dielectric contrast effect in one dimensional (1D) nanorods.[6d, 13a, 13b] The fast (~ 490 fs) rod-to-bulb exciton localization component in ZnSe/CdS nanorod can be assigned to free (untrapped) excitons. This exciton localization time is close to previously reported values in CdSe/CdS quasi-type II nanorods.[5d, 6d] The origin of the smaller (9%) and slower (~10 ps) component is unclear, although it could be attributed to excitons in shallow traps. Similar bi-phasic exciton localization process with two distinctly different rate constants has been observed in CdSe/CdS nanorods.[5d] It should be noted that because of the heterogeneities of nanorod properties (dimensions and trap densities), there are likely distributions of rates constants for these processes. Therefore, these apparent bi-phasic processes are likely a result of limited data quality and dynamic range, which prevents accurate determination of the distributions of these rate constants.

Steady State $MV^{+\bullet}$ Radial Generation

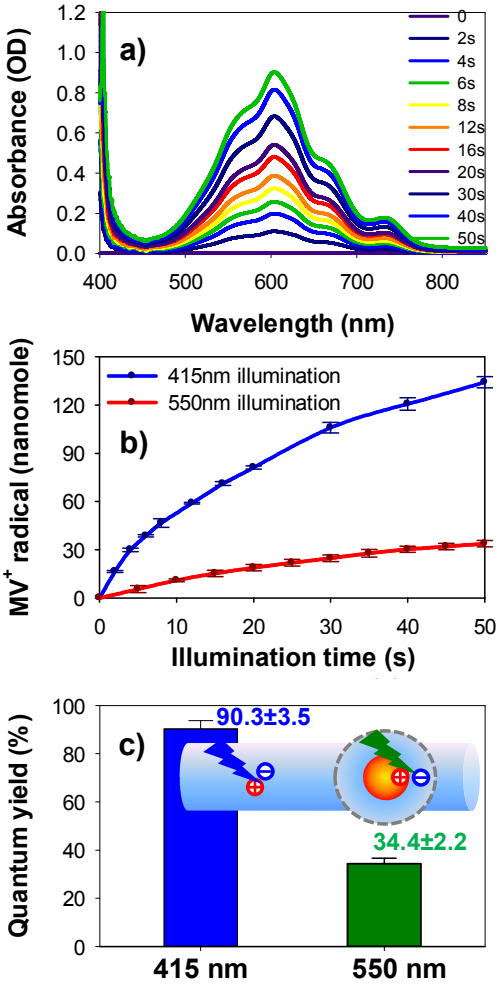

Figure 3. Steady-state photoreduction of MV^{2+} using ZnSe/CdS NRs a) UV–vis difference spectra (after–before irradiation) of a solution containing ZnSe/CdS NRs, MV^{2+} and 3-mercaptopropionic acid (MPA) after indicated duration of 415 nm illumination, showing the generation of $MV^{+\bullet}$ radicals. Similar spectra for 550 nm illumination are shown in Figure S2. Experimental conditions: 2 mM MV^{2+}, 50 mM pH 7.5 phosphate buffer, 50 mM MPA as sacrificial electron donor, total solution volume 2mL. For illuminations at 415 nm (5.09 mW) and 550 nm (5.15 mW), the concentrations of MPA-capped ZnSe/CdSe NRs were adjusted to have an absorbance of 1.46 (OD) and 0.32 (OD), respectively, at the illumination wavelengths to maintain similar photon absorption rates in these measurements. b) $MV^{+\bullet}$ radical generation kinetics under 415 and 550 nm excitations. c) Initial quantum yields of $MV^{+\bullet}$ radical generation at 415 nm and 550 nm excitation.

The presence of multiple exciton species at different regions of the nanorod and their excitation wavelength dependent branching ratios suggests wavelength dependent photochemistry. To investigate this effect, we studied MV^{2+} photoreduction using these nanorods at two illumination wavelengths: 415 nm, where the absorption of CdS rod dominates, and 550 nm, which is in resonance with the ZnSe to CdS CT band in the bulb region. The samples contain MPA capped ZnSe/CdS NRs, MV^{2+} (2 mM) and excess MPA (50 mM) as electron donor in anaerobic pH = 7.5 aqueous solutions (see S1 for details). Upon 415 nm illumination, $MV^{+\bullet}$ radicals formed quickly, as indicated by the growth of a distinct 605 nm

band in the difference spectra shown in Figure 3a (see Figure S2 for results under 550 nm illumination). Both MPA and MV^{2+} have negligible absorption in this spectral range. In the absence of NRs or illumination, no $MV^{+\bullet}$ radicals were observed. Using reported extinction coefficient (13700 ± 300 M^{-1} cm^{-1} at 605 nm)[18], the amount of $MV^{+\bullet}$ radicals can be calculated to obtain the radical concentration and formation kinetics, which are shown in Figure 3B.

To quantify and compare the photoreduction performance under 415 and 550 nm excitations, we calculated the photon-to-$MV^{+\bullet}$ conversion quantum yields, defined as $\Phi_{MV} = \Delta(MV^{+\bullet}) / \Delta(hv)$, where $\Delta(MV^{+\bullet})$ is the $MV^{+\bullet}$ radical generation rate and $\Delta(hv)$ is the photon absorption rate. The latter was calculated from the illumination power and absorbance at the illumination wavelength (see S1 for details). As seen from the slope of $MV^{+\bullet}$-vs-illumination time plots in Figure 3b, the $MV^{+\bullet}$ radical generation rate was largest at the beginning of the reaction and decreased slowly due to the consumption of electron/hole acceptors and light absorption loss from generated $MV^{+\bullet}$ radicals. Therefore, only the initial quantum yields, calculated from initial $MV^{+\bullet}$ radical generation rates (first three points), are compared in Figure 3C. Interestingly, the MV^{2+} photoreduction quantum yields were ~ 34 % under 555 nm excitation and ~ 90%, at 415 nm excitation, showing a dramatic wavelength dependence.

Charge Separation and Recombination under 555 nm Excitation

To investigate the origin of the wavelength dependent MV^{2+} photoreduction quantum yields and identify the loss mechanisms, we conducted TA measurements on the complete photoreduction systems under conditions similar to those for the steady-state MV^{2+} photoreduction (see SI for details). The NR concentrations have been increased by ~ 5 times to allow measurement in a thinner cell (1 mm). For convenience, the transient absorption measurements were conducted with 400 nm and 455 nm excitation to mimic the steady state measurements at 415 nm and 550 nm illumination, respectively. The TA spectra of reaction solution without (denoted as MPA-DIR) and with (denoted as MPA-DIR-MV) MV^{2+} at 30 ps after 555 nm excitation are compared in Figure 4a and corresponding kinetics of B2 bleach in the first 20 ps in Figure 4b. These spectra were recorded under the same single exciton excitation conditions, at which the contributions of the NRs with multiple excitons were negligible. At this excitation wavelength, the lowest energy CT exciton (B3) band in MPA capped ZnSe/CdS NRs was excited. The resulting TA spectra in the MPA-DIR sample were similar to those of ZnSe/CdS NRs in toluene (Figure 2a), showing long-lived bleaches of B2 and B3 exciton bands. Because of more pronounced scattering of the excitation light for the water soluble nanorod solution, the B3 bleach was not fully resolved and we used B2 to monitor the fate of excited electrons in NRs since they probed the same electron level.

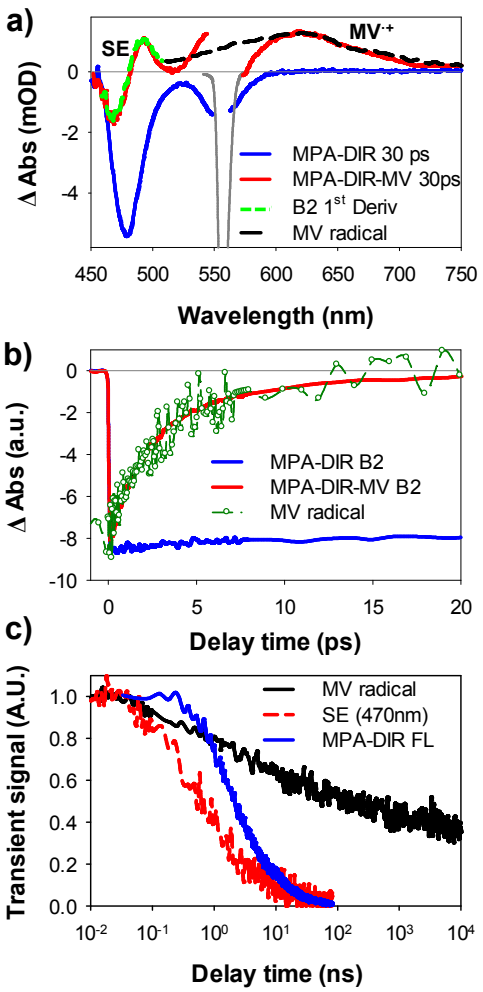

Figure 4. TA spectra and kinetics of a reaction solution under 555 nm excitation. The reaction solution was the same as that for the steady state $MV^{+\bullet}$ radical generation measurement (see Figure 2a) except for a (~5 times) higher NR concentration. a) TA spectra of MPA-capped ZnSe/CdS NR reaction solution without (blue solid line, denoted as MPA-DIR) and with (red solid line, denoted as MPA-DIR-MV) MV^{2+} at 30 ps delay time. Also shown are the spectra of the excitation pulse (dark gray line), $MV^{+\bullet}$ radical spectrum obtained from CdS QD-MV^{2+} complexes (black dashed line) and the 1st derivative of B2 absorption band (green dashed line). b) Comparison of B2 kinetics in ZnSe/CdS NRs without (blue solid line) and with (red solid line) MV^{2+}. Also shown is the $MV^{+\bullet}$ radical formation kinetics (dark green symbols), which has been scaled and displaced vertically for better comparison. c) Comparison between $MV^{+\bullet}$ radical decay kinetics (black solid line) and SE signal (470nm) (red dashed line) in MPA-DIR-MV reaction solution and fluorescence decay kinetics (blue solid line) of MPA-DIR solution.

Compared with MPA-DIR, the TA spectrum of MPA-DIR-MV at 30 ps shows a much smaller bleach amplitude and pronounced derivative feature (with a negative peak at 470 nm and a positive peak at 490 nm) at B2 exciton band, as well as an additional positive absorption band centered at ~610 nm. The broad absorption band at ~610 nm agrees well with the $MV^{+\bullet}$ radical spectrum (black dashed line in Figure 4a, obtained from CdS QD-MV^{2+} complexes) and can be assigned to the $MV^{+\bullet}$ radical. The derivative feature at B2 exciton band agrees with the 1st order derivative spectrum of B2 absorption band (green dashed line in Figure 4a) and can be assigned to Stark effect

(SE) induced exciton peak shift in the charge separated state (with the electron in $MV^{+\bullet}$ radical and hole in ZnSe seed), similar to other nanocrystal-MV^{2+} complexes.[1b, 6d, 12, 14a, 19] It will be shown below that the SE signal is dominate by the effect of the ZnSe valence band hole on the exciton bands and can be used to follow the valence band hole population in the charge separated state. As shown in Figure 4b, compared with B2 in MPA-DIR, which shows negligible bleach recovery in the first 20 ps, the B2 bleach in MPA-DIR-MV has fully recovered in the same time period, suggesting a short-lived conduction band electron in the presence of MV^{2+}. Furthermore, the B2 bleach recovery kinetics agrees well with the $MV^{+\bullet}$ radical formation kinetics in MPA-DIR-MV, indicating electron transfer from the NR to MV^{2+} molecules to form the $MV^{+\bullet}$ radicals. The $MV^{+\bullet}$ radical formation kinetics can be fitted by a single exponential function with time constant of 3.2±0.2 ps (Figure S5). Previous studies have reported non-single-exponential electron transfer kinetics from QDs to adsorbates due to heterogeneities in the number of acceptor, QD size and QD-acceptor interaction.[19b, 20] Similar heterogeneous electron transfer kinetics can be expected in our NR-MV^{2+} complexes. The apparent single exponential kinetics is likely a result of limited S/N ratio of the data. This electron transfer rate in MPA-DIR-MV is much faster (> 1000 times) than the nanosecond intrinsic lifetime of electrons in MPA-DIR, which suggests a unity QY of the initial exciton dissociation/interfacial electron transfer process if we assume that the addition of MV^{2+} to the NR sample doesn't introduce other electron loss pathways. This assumption is consistent with the high steady state quantum yield shown in Figure 3 and the near unity quantum yield reported previously for CdSe/CdS NRs.[1b] The ultrafast electron transfer rate also suggests that MV^{2+} acceptors are adsorbed on the NR surface.

The observed unity QY of initial electron transfer from NR to MV^{2+} (deduced from the measured electron transfer rate above) suggests that and the nonunity steady state MV^{2+} photoreduction QE (Figure 3) must result from charge recombination of the $MV^{+\bullet}$ radical with the hole. To monitor the $MV^{+\bullet}$ radical recombination loss, the TA kinetics of $MV^{+\bullet}$ radical and SE signal (at 470 nm) from 10 ps to 10 μs are compared in Figure 4c. The maximum value of the $MV^{+\bullet}$ radical has been normalized to one to reflect the unity yield of initial electron transfer. The normalized $MV^{+\bullet}$ radical signal amplitude represents the time dependent transient QY in the reaction solution, reflecting the extent of recombination loss. The $MV^{+\bullet}$ radical transient QY decreases gradually with time, showing a half-life time of ~ 170 ns. The transient QY is ~ 38% at 10 μs, close to the steady state MV^{2+} photoreduction quantum yield, indicating that the charge recombination loss is the main cause for low steady state quantum yield under 550 nm illumination.

The lifetime of the $MV^{+\bullet}$ radical is determined by the competition between back electron transfer from the radical to the hole in ZnSe valence band (i.e. charge recombination) and hole removal by electron donors. The latter process can be probed by the band edge fluorescence decay kinetics of MPA-DIR, as shown in Figure 4c. Because transient absorption kinetics of MPA-DIR shows a long lived CB electron with a half-life time of ~ 10 ns, the measured PL decay can be attributed to the removal of ZnSe valence band holes by MPA.[1b, 3e] The fluorescence decay shows a half-life time of ~ 2 ns, which is ~ 4 time longer than the previously reported value in ZnSe/CdS NRs,[3e] probably due to a thicker CdS shell surrounding the ZnSe seed in our ZnSe/CdS NRs. The intrinsic charge recombination rate of the $MV^{+\bullet}$ radical with the hole in ZnSe valence band can also be measured in ZnSe/CdS-MV^{2+} complexes, in the absence of electron donor. As shown in Figure S3, the SE signal shows identical decay kinetics as $MV^{+\bullet}$ radical with a half-life time of ~ 22 ns, reflecting the charge recombination process between the VB hole in ZnSe seed and the electron in $MV^{+\bullet}$ radical.

As shown in Figure 4c, the SE signal decay is faster than the decay of $MV^{+\bullet}$ radicals in MPA-DIR-MV and the PL decay in MPA-DIR. It suggests that the charge separation induced SE signal is due to the presence of holes in the ZnSe seed, instead of electrons in $MV^{+\bullet}$ radical. This assignment is further supported below in the kinetics measured with 400 nm excitation, in which we show that the SE decay follows the hole removal kinetics by MPA while the $MV^{+\bullet}$ radical show negligible decay during the same time period. Under 550 nm excitation, the SE decay in MPA-DIR-MV contains the contributions of ZnSe valence band hole removal by both transfer to MPA and charge recombination with $MV^{+\bullet}$ radicals. As a result, the SE signal decays faster than the $MV^{+\bullet}$ radical decay in MPA-DIR-MV and PL decay in MPA-DIR. It should be pointed out that the loss of $MV^{+\bullet}$ radical persisted even after the complete removal of ZnSe valence band holes (monitored by SE decay), suggesting recombination with the trapped holes or oxidized MPA molecules on hundreds of nanosecond time scale. The short spatial separation of the electron (in $MV^{+\bullet}$ radicals) and hole (in ZnSe seeds or oxidized MPA) in the charge separate state is the key reason for the relatively low steady state quantum yield of MV^{2+} photoreduction under 555 nm excitation.

Charge Separation and Recombination under 400 nm Excitation

Shown in Figure 5 are the comparison of TA spectra and kinetics in MPA-DIR and MPA-DIR-MV measured with 400 nm excitation. These spectra were recorded under the same single exciton excitation conditions. As shown in Supporting Information S6, MPA-DIR in water shows similar TA spectra and B1, B2, B3 kinetics as DIR in toluene (without MPA) in the first 50 ps. Therefore, the early time exciton localization dynamics for MPA capped NRs in water are similar to ZnSe/CdS NRs in toluene discussed above. At later delay time, the exciton bleach decay kinetics for MPA-DIR is faster than NRs in toluene, which may be attributed to faster electron trapping or electron-hole recombination caused by the ligand exchange process. Compared with MPA-DIR, the B1 bleach in MPA-DIR-MV had a smaller (~ 58%) initial amplitude and

nearly completely recovered in the first ~ 1 ps; the B2 (B3) bleach showed an initial amplitude of only ~ 14% of the free NR and a relatively slow decay on the a few ps time scale. The decay of these exciton bleaches was accompanied by the formation of derivative-like Stark effect features at those exciton bands and a $MV^{+\bullet}$ radical absorption band at 600 nm. These spectral signatures are similar to those observed under 555nm excitation and can be also attributed to electron transfer from the NR to the MV^{2+} molecules.

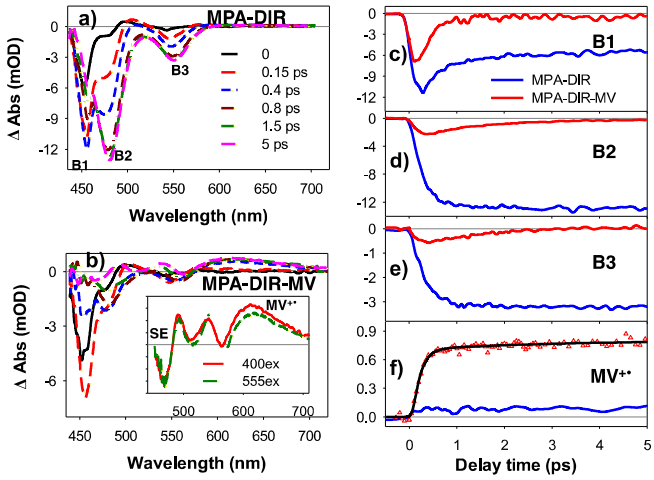

Figure 5. TA spectra and kinetics of reaction solution at 0 - 5 ps after 400 nm excitation. The reaction solution is same as that for steady state MV radical generation except for a higher (~ 5 times) NR concentration. (a, b) TA spectra of MPA-capped ZnSe/CdS DIR reaction solution without (a) and with (b) MV^{2+} at indicated delay times. Inset in Figure b: comparison of TA spectra at 30 ps measured with 400 nm and 555 nm excitation. (c, d, e, f) Comparison of B1, B2, B3 and $MV^{+\bullet}$ kinetics (615nm) between MPA-DIR and MPA-DIR-MV.

The $MV^{+\bullet}$ radical formation kinetics can be fitted by a biexponential function with amplitudes and time constants of (87±3%, 132±23 fs) and (13±3%, 3.0±0.4 ps), respectively. The electron transfer time of the fast component is ~ 4 times faster than the exciton localization time from the CdS rod to the bulb region, suggesting that 87% of the exciton generated in CdS rod undergoes ultrafast transfer to MV^{2+} before exciton localization. For the slower $MV^{+\bullet}$ radical growth component, its percentage agrees with initial amplitude of B2/B3 bleach and its formation time is the same as the electron transfer time from the conduction band 1Se level of the bulb region, which has been measured with 555 nm excitation (Figure 4). This indicates that in MPA-DIR-MV, only ~ 13% of the excitons initially generated in CdS rod localizes into the bulb region where they dissociate by electron transfer (~ 3 ps) to MV^{2+} molecules. The much faster electron transfer rate from CdS rod than from the bulb region can be attributed to a larger quantum confinement along radial direction in the CdS rod region.

These results suggest that excitons generated in the CdS rod region of ZnSe/CdS NRs have three charge separation pathways, which are summarized in Figure 6. Because of ultrafast electron transfer from the CdS nanorod to MV^{2+} (faster than exciton localization), under the presence of MV^{2+}, only 13% of the excitons localizes to the ZnSe/CdS bulb region, where they dissociate by electron transfer to MV^{2+} with a time constant of ~3 ps to form charge separated state A. The other 87% of the excitons undergoes ultrafast electron transfer (~132 fs) to MV^{2+} adsorbed on the CdS rod. Among them, 17 %, which are trapped on CdS rod due to hole trapping, leads to charge separated state B. The remaining 70% generates holes in the valence band of CdS rod, which is followed by rapid localization to the ZnSe seed because of the valance band offset. This pathway produces a charge-separated state C with a much larger distance between the electron (in $MV^{+\bullet}$ radical) and the hole (in ZnSe or MPA ligand surrounding the bulb). Here we have assumed that the adsorption of MV^{2+} does not affect the hole trapping rate on CdS rods.

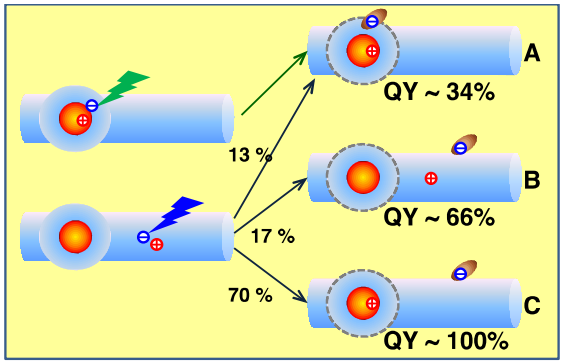

Figure 6. Schematic depiction of charge separated states A, B and C generated in MPA-DIR-MV complexes after excitation at the bulb and rod regions. A: hole localized in ZnSe and electron transferred to MV^{2+} adsorbed on the bulb region. B and C: electron transferred to MV^{2+} adsorbed on the rod region with the hole trapped in the CdS rod (B) and localized in the ZnSe seed (C). Also shown is the branching ratios of these pathways and their steady state quantum yields for MV^{2+} photoreduction.

This model is further supported by a comparison of charge separated state spectra at 30 ps measured with 400 and 555 nm excitations (inset of Figure 5b). At this delay time, charge separation process is completed and the charge recombination and hole removal processes haven't started yet. It shows a ~ 20% smaller SE signal for the spectrum measured at 400 nm excitation. Because of the 1:1 relationship between $MV^{+\bullet}$ radical and ZnSe seed localized hole (which leads to SE signal) at 555 nm excitation, the smaller SE signal at 400 nm excitation suggests only 80% of the hole is localized at ZnSe seed, consistent with the branching ratios to pathway A and C, while 20% of the hole is trapped on the CdS rod domain, corresponding to pathway B. Because of the strongly localized nature of trapped holes on CdS rod and their spatial separation from the seed region in ZnSe/CdS nanorod, they have negligible contribution to the B2 Stark effect signal in the charge separated state.

The ultrafast exciton dissociation and $MV^{+\bullet}$ radical formation kinetics shown in Figure 5 suggests a unity initial $MV^{+\bullet}$ radical generation QY at 400 nm excitation. To explain the steady state QY shown in Figure 3, we again measured the TA spectra of MPA-DIR-MV up to 10 μs after 400 nm

excitation to monitor the charge recombination loss. The TA spectra from 0.05 ns to 10 μs are shown in Figure 7a, which shows the pronounced SE signal and $MV^{+\bullet}$ radical absorption from charge separated states. The normalized comparison of the kinetics of SE signal at 470 nm and $MV^{+\bullet}$ radical signal at 610 nm are shown in Figure 7b. Also compared is the band edge PL decay kinetics of MPA-DIR, which monitors the removal of ZnSe valence band hole by MPA molecules. SE decay in MPA-DIR-MV agrees with the PL decay kinetics of MPA-DIR, with a half-life time of ~ 2 ns. This agreement indicates that SE signal is caused mainly by the holes in ZnSe seed and hole transfer to MPA is the dominant hole decay pathway in MPA-DIR-MV at 400 nm excitation. The $MV^{+\bullet}$ radical decays much more slowly compared to the kinetics measured with 555 nm excitation. The transient QY at 10 μs is 88%, which is consistent with the high steady state QY (90%, Figure 3) and indicates an efficient suppression of the charge recombination process at this excitation wavelength. As will be discussed below, efficient suppression of charge recombination can be attributed to the presence of longer distance charge separated state (pathways B and C) upon the excitation of the CdS rod region.

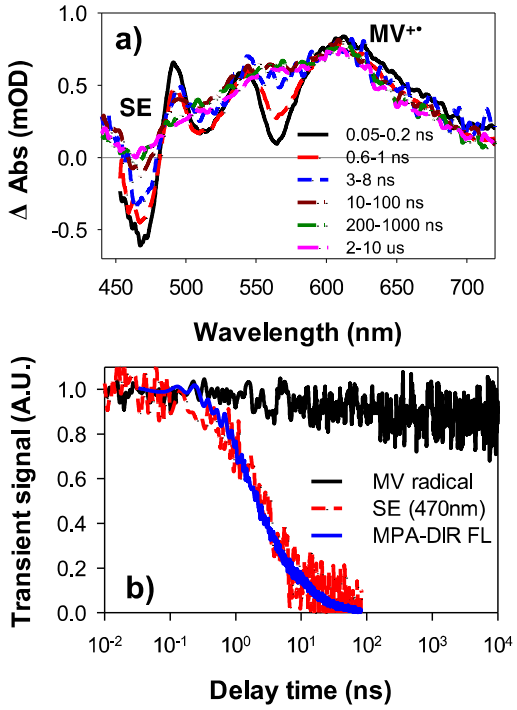

Figure 7. TA spectra and kinetics of reaction solution at 0.05 ns - 10 μs after 400 nm excitation. a) TA spectra of MPA-DIR-MV at indicated delay times b) Comparison of $MV^{+\bullet}$ radical decay kinetics (black solid line) and SE signal (470nm) (red dashed line) in MPA-DIR-MV reaction solution and fluorescence decay kinetics of MPA-DIR solution (blue solid).

Mechanism of Wavelength Dependent MV^{2+} Photoreduction Yield

The time-resolved studies of the elementary steps involved in the overall MV^{2+} photoreduction reaction provide insight into the mechanisms for wavelength dependent $MV^{+\bullet}$ radical generation QY under steady state illumination. As shown in Figure 6, direct excitation of the bulb region at 550 nm (or wavelength longer than B2), generate charge transfer excitons in the bulb region with holes confined in ZnSe seed and electrons localized in the CdS bulb. These excitons dissociate by electrons transfer (~ 3 ps) to adsorbed MV^{2+} molecules with unity quantum yield. Due to the proximity of the electrons with the holes left in ZnSe seed (or transferred thiol), the charge recombination loss is high, leading to relatively small steady $MV^{+\bullet}$ radical generation QY (~35%). As discussed above, TA study at 400 nm (Figure 5) reveals that illumination at B1 or shorter wavelength generates excitons in CdS nanorod domain that undergo three pathways of charge separation. As shown in Figure 6, the CS state in pathway A (13%) is similar to the direct excitation of the CT band, which should lead to a steady state $MV^{+\bullet}$ radical generation QY of 34%, similar to that measured at 550 nm excitation. Pathway B (17%) is similar to that observed in CdS rod (without the ZnSe seed), the QY of which is estimated to be ~ 66% based on a previous measurement of CdS rods.[1b] The remaining 70% of excitons proceed by pathway C, which generates a charge separated state with long e-h spatial distance to effectively suppress charge recombination loss. Assuming a $MV^{+\bullet}$ radical generation QYs of 100% for pathway C, we can estimate a total quantum yield of ~86% for 400 nm illumination, which is close to the measured value (90%).

Similar competition of exciton trapping on CdS rod and localization to seed region has also been observed in CdSe/CdS NRs and rod-to-seed exciton localization efficiency ranging from ~53% to unity has been reported by different groups.[6d, 9a, 16] We previously observed near unity quantum efficiency of $MV^{+\bullet}$ radical photogeneration using CdSe/CdS nanorods, which suggests that pathway C is the dominating charge transfer process in that sample.[1b] This difference may be attributed to sample dependent branching ratios among the multiple pathways, which likely depend on the synthetic conditions (trap density and distribution), nanorod shape and dimensions (size and length of the rod, as well as the size of seed and shell thickness of the bulb region),[6d, 9a, 16] and variation of electron acceptor binding affinities in different region of the NR. Furthermore, in the presence of catalysts, these $MV^{+\bullet}$ radical photogeneration systems can be used for light-driven H_2 evolution[1b, 7] or CO_2 reduction.[8] Therefore, wavelength dependent quantum yields of photocatalysis can be expected in systems that employ these nanorods as light harvesting components.

Further optimization of the system can be achieved by enhancing the branching ratio of pathway C and/or improving the efficiencies of pathways A and B. Through selective etching of CdS outer shell in the bulb region,[3d] the removal of the hole in the seed by electron donor can be enhanced, which should improve the $MV^{+\bullet}$ generation efficiency for pathway A.[3d]

Trapping of excitons on CdS nanorod surface represent another major loss. Surface passivation (e.g. Cd^{2+} layer termination) to remove the hole trapping sites could be one way to reduce the contribution of pathway B.[21] In addition, it is found that shorter nanorods and nanotetrapod heterostructures can decrease exciton trapping in the CdS rod domain,[9a] which can also boost the efficiency of this redox mediator based solar-to-fuel conversion approach. The high efficiency of pathway C requires ultrafast electron transfer to acceptors to compete with fast exciton localization to the seed region. To achieve efficient charge separation to acceptors with slow electron transfer rates (such as catalysts), it would be helpful to explore more sophisticated nanoheterostructures that are designed for long distance electron and hole separation within the nanoheterostrutures.

Conclusions

We have investigated the wavelength dependent exciton localization and photoreduction mechanisms in type II ZnSe/CdS dot-in-rod nanorod heterostructures by transient absorption spectroscopy and time-resolved fluorescence decay. It was shown that excitation of the lowest energy charge transfer band generated a long-lived exciton state with the hole localized in the ZnSe seed and electron localized in the surrounding CdS bulb region. Despite the type II band alignment, the conduction band electron did not extend substantially to the CdS rod, which was likely caused by smaller diameter (larger electron confinement energy) of the latter region and strong Coulomb interaction with the hole in the ZnSe seed. For ZnSe/CdS nanorods studied here, 83% of excitons generated in the CdS rod localized rapidly to the charge transfer exciton state in the seed/bulb region and the remaining 17% remained in the CdS rod, likely caused by rapid hole trapping.

Under continuous illumination in the presence of MPA electron donor, the wavelength dependent exciton distribution led to dramatic wavelength dependent steady state QY of MV^{2+} photoreduction in aqueous solution: 34% and 90% for 550 nm and 415 nm excitation, respectively. Direct excitation of charge transfer exciton band at 550 nm created excitons in the bulb region, whose dissociation by electron transfer to MV^{2+} generated charge separated state A with the hole in the ZnSe seed and electron in $MV^{+\bullet}$ radical adsorbed in the bulb region. The spatial proximity of the electron and hole gave rise to large recombination loss, accounting for the lower steady state QY of MV^{2+} photoreduction at 550 nm illumination. Excitation of the CdS rod led to three types of charge separated states. The majority of excitons (70%) dissociated by ultrafast electron transfer to MV^{2+}, followed by rapid hole localization into the ZnSe seed to generate charge separated state C. Due to the large spatial separation of the electrons (in $MV^{+\bullet}$ adsorbed on the rod region) and holes (localized in the seed), this charge separated state suppressed recombination, leading to near unity steady state quantum yield of MV^{2+} photoreduction. The remaining pathways generated charge-separated states with both electrons and holes in the bulb/seed region (A) or in the rod region (B). The smaller e-h spatial separation in these pathways led to larger recombination loss and lower steady-state quantum yield. Since competition among these pathways is likely a general property, the observed wavelength dependent exciton distribution and photocatalysis QY can also be expected in many other linear and branched nanoheterostructures (e.g. Cd or Zn based nanorod, nanowires, tetrapods, dumbbells). Furthermore, the branching ratios among these competing pathways depend on the synthetic conditions and shapes and dimensions of the nanoheterostructures, which suggests possible approaches for rational improvement of their performance in light-harvesting and charge separation applications.

Acknowledgements

This work was funded by the U.S. Department of Energy, Office of Basic Energy Sciences, Solar Photochemistry Program (DE-FG02-12ER16347).

Notes and References

Department of Chemistry, Emory University, Atlanta, Georgia 30322, United States.
Email: tlian@emory.edu

Electronic Supplementary Information (ESI) available: Experimental details, fitting model and parameters, nanosecond TA spectra and kinetics of ZnSe/CdS under 400 nm excitation, UV-Vis difference spectra of $MV^{+\bullet}$ radical generation under 550 illumination. See DOI: 10.1039/b000000x/

1. (a) H. Zhu and T. Lian, *Energy Environ. Sci.*, 2012, **5**, 9406-9418; (b) H. Zhu, N. Song, H. Lv, C. L. Hill and T. Lian, *J. Am. Chem. Soc.*, 2012, **134**, 11701-11708; (c) M. B. Wilker, K. J. Schnitzenbaumer and G. Dukovic, *Isr. J. Chem.*, 2012, **52**, 1002-1015; (d) B. L. Greene, C. A. Joseph, M. J. Maroney and R. B. Dyer, *J. Am. Chem. Soc.*, 2012, **134**, 11108-11111; (e) K. A. Brown, M. B. Wilker, M. Boehm, G. Dukovic and P. W. King, *J. Am. Chem. Soc.*, 2012, **134**, 5627-5636; (f) M. J. Berr, F. F. Schweinberger, M. Döblinger, K. E. Sanwald, C. Wolff, J. Breimeier, A. S. Crampton, C. J. Ridge, M. Tschurl, U. Heiz, F. Jäckel and J. Feldmann, *Nano Lett.*, 2012, **12**, 5903-5906; (g) Z. Han, F. Qiu, R. Eisenberg, P. L. Holland and T. D. Krauss, *Science*, 2012, **338**, 1321-1324; (h) J. Huang, K. L. Mulfort, P. Du and L. X. Chen, *J. Am. Chem. Soc.*, 2012, **134**, 16472-16475; (i) L. Amirav and A. P. Alivisatos, *J. Phys. Chem. Lett.*, 2010, **1**, 1051-1054.
2. (a) S. S. Lo, T. Mirkovic, C.-H. Chuang, C. Burda and G. D. Scholes, *Adv. Mater.*, 2011, **23**, 180-197; (b) R. Costi, A. E. Saunders and U. Banin, *Angew. Chem. Int. Ed.*, 2010, **49**, 4878-4897; (c) C. d. M. Donega, *Chem. Soc. Rev.*, 2011, **40**, 1512-1546.
3. (a) K. P. Acharya, R. S. Khnayzer, T. O'Connor, G. Diederich, M. Kirsanova, A. Klinkova, D. Roth, E. Kinder, M. Imboden and M. Zamkov, *Nano Lett.*, 2011, **11**, 2919-2926; (b) M. L. Tang, D. C. Grauer, B. Lassalle-Kaiser, V. K. Yachandra, L. Amirav, J. R. Long, J. Yano and A. P. Alivisatos, *Angew. Chem. Int. Ed.*, 2011, **50**,

10203-10207; (c) P. Tongying, V. V. Plashnitsa, N. Petchsang, F. Vietmeyer, G. J. Ferraudi, G. Krylova and M. Kuno, *J. Phys. Chem. Lett.*, 2012, 3234-3240; (d) E. Khon, K. Lambright, R. S. Khnayzer, P. Moroz, D. Perera, E. Butaeva, S. Lambright, F. N. Castellano and M. Zamkov, *Nano Lett.*, 2013, **13**, 2016-2023; (e) T. O'Connor, M. S. Panov, A. Mereshchenko, A. N. Tarnovsky, R. Lorek, D. Perera, G. Diederich, S. Lambright, P. Moroz and M. Zamkov, *ACS Nano*, 2012, **6**, 8156-8165.

4. (a) D. Steiner, D. Dorfs, U. Banin, F. Della Sala, L. Manna and O. Millo, *Nano Lett.*, 2008, **8**, 2954-2958; (b) D. Dorfs, A. Salant, I. Popov and U. Banin, *Small*, 2008, **4**, 1319-1323; (c) N. N. Hewa-Kasakarage, M. Kirsanova, A. Nemchinov, N. Schmall, P. Z. El-Khoury, A. N. Tarnovsky and M. Zamkov, *J. Am. Chem. Soc.*, 2009, **131**, 1328-1334; (d) S. A. Ivanov, A. Piryatinski, J. Nanda, S. Tretiak, K. R. Zavadil, W. O. Wallace, D. Werder and V. I. Klimov, *J. Am. Chem. Soc.*, 2007, **129**, 11708-11719.
5. (a) J. Müller, J. M. Lupton, P. G. Lagoudakis, F. Schindler, R. Koeppe, A. L. Rogach, J. Feldmann, D. V. Talapin and H. Weller, *Nano Lett.*, 2005, **5**, 2044-2049; (b) J. Müller, J. M. Lupton, A. L. Rogach, J. Feldmann, D. V. Talapin and H. Weller, *Phys. Rev. B*, 2005, **72**, 205339; (c) M. G. Lupo, F. Della Sala, L. Carbone, M. Zavelani-Rossi, A. Fiore, L. Lüer, D. Polli, R. Cingolani, L. Manna and G. Lanzani, *Nano Lett.*, 2008, **8**, 4582-4587; (d) C. She, A. Demortière, E. V. Shevchenko and M. Pelton, *J. Phys. Chem. Lett.*, 2011, 1469-1475; (e) A. Sitt, F. D. Sala, G. Menagen and U. Banin, *Nano Lett.*, 2009, **9**, 3470-3476; (f) Y. Luo and L.-W. Wang, *ACS Nano*, 2009, **4**, 91-98; (g) R. M. Kraus, P. G. Lagoudakis, A. L. Rogach, D. V. Talapin, H. Weller, J. M. Lupton and J. Feldmann, *Phys. Rev. Lett.*, 2007, **98**, 017401; (h) M. Grazia Lupo, F. Scotognella, M. Zavelani-Rossi, G. Lanzani, L. Manna and F. Tassone, *Phys. Chem. Chem. Phys.*, 2012, **14**, 7420-7426.
6. (a) H. Eshet, M. Grünwald and E. Rabani, *Nano Lett.*, 2013, **13**, 5880-5885; (b) L. T. Kunneman, M. Zanella, L. Manna, L. D. A. Siebbeles and J. M. Schins, *J. Phys. Chem. C*, 2013, **117**, 3146-3151; (c) G. Rainò, T. Stöferle, I. Moreels, R. Gomes, J. S. Kamal, Z. Hens and R. F. Mahrt, *ACS Nano*, 2011, **5**, 4031-4036; (d) K. Wu, W. E. Rodríguez-Córdoba, Z. Liu, H. Zhu and T. Lian, *ACS Nano*, 2013, **7**, 7173-7185; (e) C. Mauser, E. Da Como, J. Baldauf, A. L. Rogach, J. Huang, D. V. Talapin and J. Feldmann, *Phys. Rev. B*, 2010, **82**, 081306.
7. (a) J. Kiwi and M. Gratzel, *Nature*, 1979, **281**, 657-658; (b) I. Okura, N. Kim-Thuan and M. Takeuchi, *Angew. Chem. Int. Ed. Engl.*, 1982, **21**, 434-435.
8. (a) B. A. Parkinson and P. F. Weaver, *Nature*, 1984, **309**, 148-149; (b) W. Shin, S. H. Lee, J. W. Shin, S. P. Lee and Y. Kim, *J. Am. Chem. Soc.*, 2003, **125**, 14688-14689.
9. (a) D. V. Talapin, J. H. Nelson, E. V. Shevchenko, S. Aloni, B. Sadtler and A. P. Alivisatos, *Nano Lett.*, 2007, **7**, 2951-2959; (b) L. Carbone, C. Nobile, M. De Giorgi, F. D. Sala, G. Morello, P. Pompa, M. Hytch, E. Snoeck, A. Fiore, I. R. Franchini, M. Nadasan, A. F. Silvestre, L. Chiodo, S. Kudera, R. Cingolani, R. Krahne and L. Manna, *Nano Lett.*, 2007, **7**, 2942-2950.
10. N. J. Borys, M. J. Walter, J. Huang, D. V. Talapin and J. M. Lupton, *Science*, 2010, **330**, 1371-1374.
11. (a) S. Kim, B. Fisher, H. J. Eisler and M. Bawendi, *J. Am. Chem. Soc.*, 2003, **125**, 11466-11467; (b) A. Nemchinov, M. Kirsanova, N. N. Hewa-Kasakarage and M. Zamkov, *J. Phys. Chem. C*, 2008, **112**, 9301-9307; (c) H. Zhu, N. Song and T. Lian, *J. Am. Chem. Soc.*, 2011, **133**, 8762-8771.
12. K. Wu, H. Zhu, Z. Liu, W. Rodríguez-Córdoba and T. Lian, *J. Am. Chem. Soc.*, 2012, **134**, 10337-10340.
13. (a) A. Shabaev and A. L. Efros, *Nano Lett.*, 2004, **4**, 1821-1825; (b) F. Vietmeyer, M. P. McDonald and M. K. Kuno, *J. Phys. Chem. C*, 2012, **116**, 12379-12396; (c) J. Giblin and M. Kuno, *J. Phys. Chem. Lett.*, 2010, **1**, 3340-3348.
14. (a) H. Zhu, N. Song, W. Rodríguez-Córdoba and T. Lian, *J. Am. Chem. Soc.*, 2012, **134**, 4250-4257; (b) C.-H. Chuang, T. L. Doane, S. S. Lo, G. D. Scholes and C. Burda, *ACS Nano*, 2011, **5**, 6016-6024; (c) F. Scotognella, K. Miszta, D. Dorfs, M. Zavelani-Rossi, R. Brescia, S. Marras, L. Manna, G. Lanzani and F. Tassone, *J. Phys. Chem. C*, 2011, **115**, 9005-9011; (d) N. N. Hewa-Kasakarage, P. Z. El-Khoury, A. N. Tarnovsky, M. Kirsanova, I. Nemitz, A. Nemchinov and M. Zamkov, *ACS Nano*, 2010, **4**, 1837-1844; (e) C. She, G. W. Bryant, A. Demortière, E. V. Shevchenko and M. Pelton, *Phys. Rev. B*, 2013, **87**, 155427.
15. (a) V. I. Klimov, *J. Phys. Chem. B*, 2000, **104**, 6112-6123; (b) V. I. Klimov, *Annu. Rev. Phys. Chem.*, 2007, **58**, 635-673.
16. J. I. Wong, N. Mishra, G. Xing, M. Li, S. Chakrabortty, T. C. Sum, Y. Shi, Y. Chan and H. Y. Yang, *ACS Nano*, 2014, **8**, 2873-2879.
17. A. A. Lutich, C. Mauser, E. Da Como, J. Huang, A. Vaneski, D. V. Talapin, A. L. Rogach and J. Feldmann, *Nano Lett.*, 2010, **10**, 4646-4650.
18. T. Watanabe and K. Honda, *J. Phys. Chem.*, 1982, **86**, 2617-2619.
19. (a) H. Zhu and T. Lian, *J. Am. Chem. Soc.*, 2012, **134**, 11289-11297; (b) A. J. Morris-Cohen, M. T. Frederick, L. C. Cass and E. A. Weiss, *J. Am. Chem. Soc.*, 2011, **133**, 10146-10154.
20. (a) A. Boulesbaa, A. Issac, D. Stockwell, Z. Huang, J. Huang, J. Guo and T. Lian, *J. Am. Chem. Soc.*, 2007, **129**, 15132-+; (b) J. Huang, Z. Huang, S. Jin and T. Lian, *J. Phys. Chem. C*, 2008, **112**, 19734-19738; (c) S. Jin, J. C. Hsiang, H. Zhu, N. Song, R. M. Dickson and T. Lian, *Chem Sci*, 2010, **1**, 519-526; (d) N. Song, H. Zhu, S. Jin, W. Zhan and T. Lian, *ACS Nano*, 2011, **5**, 613-621; (e) H. Zhu, Y. Yang, K. Hyeon-Deuk, M. Califano, N. Song, Y. Wang, W. Zhang, O. V. Prezhdo and T. Lian, *Nano Lett.*, 2014, **14**, 1263-1269; (f) K. E. Knowles, M. Malicki and E. A. Weiss, *J. Am. Chem. Soc.*, 2012.
21. H. H.-Y. Wei, C. M. Evans, B. D. Swartz, A. J. Neukirch, J. Young, O. V. Prezhdo and T. D. Krauss, *Nano Lett.*, 2012, **12**, 4465-4471.

